High-Mass-Loading CoNi-Layered Double Hydroxide Directly Grown on Brush-like Cu/Carbon Cloth as High-Areal-Capacitance Supercapacitor Electrode

Yichen Feng,[a] Zhuang Yang,[a] Yu-Hung Fang,[b] Ying-Chu Chen,*[a] and Yu-Kuei Hsu*[b]

A combination of high mass loading and efficient utilization of electroactive materials is crucial for simultaneously enhancing the energy and power densities of energy storage devices. This is exemplified herein using cobalt nickel layered double hydroxides nanosheets (CoNi-LDHs) directly grown on copper nanowires (Cu NWs) standing quasi-vertically on carbon cloth (CC) to yield a multi-core-shell CoNi-LDHs/Cu NWs/CC as the supercapacitor electrode that exhibits a high areal capacitance of 5.55 F cm^{-2} (corresponding to a gravimetric capacitance of 1209.15 F g^{-1}) at a large current density of 10 mA cm^{-2}. Such superior rate capability is attributed to the high packing density of CoNi-LDHs in the electrode, benefitting from the large specific surface area of Cu NWs/CC. Additional contribution stems, on the other hand, from the facile charge transfer kinetics resulted from the elimination of binder from the electrode coupled with the mesopores between not only Cu NWs but also CoNi-LDHs nanosheets, and the macropores between the carbon fiber of CC. Benefitting from such exceptional rate performance is the supercapacitor built on CoNi-LDHs/Cu NWs/CC as the positive electrode coupled with bismuth subcarbonate (Bi$_2$O$_2$CO$_3$) as the negative electrode capable of delivering outstanding power density of 13.31 mW cm^{-2} and energy density of 0.35 mWh cm^{-2}.

Introduction

Due to its outstanding capability of balancing the demands for high energy density and good rate performance, pseudocapacitor has long been a hot topic under intensive investigation in the energy storage field.[1–6] Not only a variety of pseudocapacitive materials, for example the transition metal oxides and conductive polymers, etc., have been developed, but also their capacitance has been largely enhanced to approach the theoretical value.[7–11] Such improvements are, however, mostly limited to laboratory devices using ultrathin electrodes with extremely low mass loadings usually no more than 1 mg cm^{-2}.[12–15] Taking into account of the real device containing not only those electroactive materials but also additional components, for example the current collector, the separator, among others, which do not actively contribute to the charge storage but for the cost and weight, their outstanding gravimetric capacitance is in this regard hardly translated to the gravimetric energy and power densities of the pseudocapacitors.[16–18] To address this issue by increasing the packing density of pseudocapacitive materials at the expense of the aforesaid passive elements, nevertheless, remains impractical. This is attributed to the electrode thickness being in the meantime augmented due to its planar architecture, through which is the ion diffusion largely impeded, leading to severe deteriorations in specific capacitance and rate performance.[19–21] Worse yet, as an additional result of such two-dimensional electrode configuration is the limited contact of the electroactive materials with the underlying metal foil as the current collector. This highly likely results in their delamination during the roll-to-roll and drying process. Moreover, this along with their poor electrical conductivity collectively render the cell impedance markedly increased to in turn further impair the device performance.[22–24] To tackle those challenges, an alternative nonplanar current collector with not only large specific surface area but also high porosity is required.[25–27] On the one hand, it can effectively interface with the pseudocapacitive materials even at high mass loading to in this way facilitate the electron transport and enhance their stability. On the other hand, the infiltration of the electrolyte through the entire electrode is also promoted. A variety of electrode supports have in view of such strong thirst been put forward, among which is the carbon cloth (CC) preferentially chosen in the present contribution due to its capability of meeting the aforementioned demands.[28–30] On the other hand, its lightweight ($\sim$12 mg cm^{-2}) and flexibility highly likely further extend the application frontier of pseudocapacitors to new domains, for example the portable and wearable electronics. Of particular note are those copper nanowires (Cu NWs) standing vertically on CC, giving rise to Cu NWs/CC with not only a brush-like microtexture but also numerous mesopores between adjacent Cu NWs. This along with that formed between CoNi-LDHs as a result of their morphologic engineering into a sheet-like

[a] Y. Feng, Z. Yang, Prof. Dr. Y.-C. Chen
China-UK Low Carbon College
Shanghai Jiao Tong University
No. 3, Yinlian Road, Lingang, Shanghai, 201306, People's Republic of China
E-mail: ying-chu.chen@sjtu.edu.cn

[b] Y.-H. Fang, Prof. Dr. Y.-K. Hsu
Department of Opto-Electronic Engineering
National Dong Hwa University
No. 1, Sec. 2, Da Hsueh Road, Shoufeng, Hualien, 97401, Taiwan
E-mail: ykhsu@gms.ndhu.edu.tw

Supporting information for this article is available on the WWW under https://doi.org/10.1002/batt.202300068

nanostructure and the macropores between the carbon fibers of CC collectively result in a hierarchical porous network to facilitate the penetration of the electrolyte through the CoNi-LDHs/Cu NWs/CC electrode. Herein, CoNi-LDHs are preferentially chosen as the electroactive material in view of their outstanding electrochemical properties, as evidently reflected in their specific capacitance readily exceeding 1,000 $F g^{-1}$.[31–35] The synergistic effect of such facile electron conduction and rapid ion diffusion renders the CoNi-LDHs/Cu NWs/CC electrode exhibiting an outstanding areal capacitance amounting to 5.55 $F cm^{-2}$ (corresponding to a gravimetric capacitance of 1209.15 $F g^{-1}$) at a high current density of 10 $mA cm^{-2}$. This far surpasses those reported for additional pseudocapacitive materials in the literature.[36–39] Most importantly, benefitting from such superior performance is the asymmetric pseudocapacitor built on CoNi-LDHs/Cu NWs/CC functioned as the positive electrode coupled with the bismuth subcarbonate $((BiO)_2CO_3)$ worked as the negative electrode capable of delivering remarkable energy density of 0.352 $mWh cm^{-2}$ and power density of 13.311 $mW cm^{-2}$. These device performances

also well excel those of additional hybrid and pseudocapacitors reported in the literature.[14,40–42] The great promise of the electrode design developed in this study with the careful consideration of the requirements from a device perspective is in view of the aforementioned outperformance well corroborated. This blueprint can serve as an important guidance for future development of additional electrodes with high mass loading for practical energy storage applications.

Results and Discussion

Structural and compositional characterizations of CoNi-LDHs/Cu NWs/CC

The SEM images of pristine CC, Cu NWs/CC and CoNi-LDHs/Cu NWs/CC are plotted alongside in Figure 1(b–d) for comparison to in this way highlight the morphologic evolution resulted from the consecutive electrodeposition of CoNi-LDHs and Cu NWs on CC. The major discrepancy among them lies in, on the
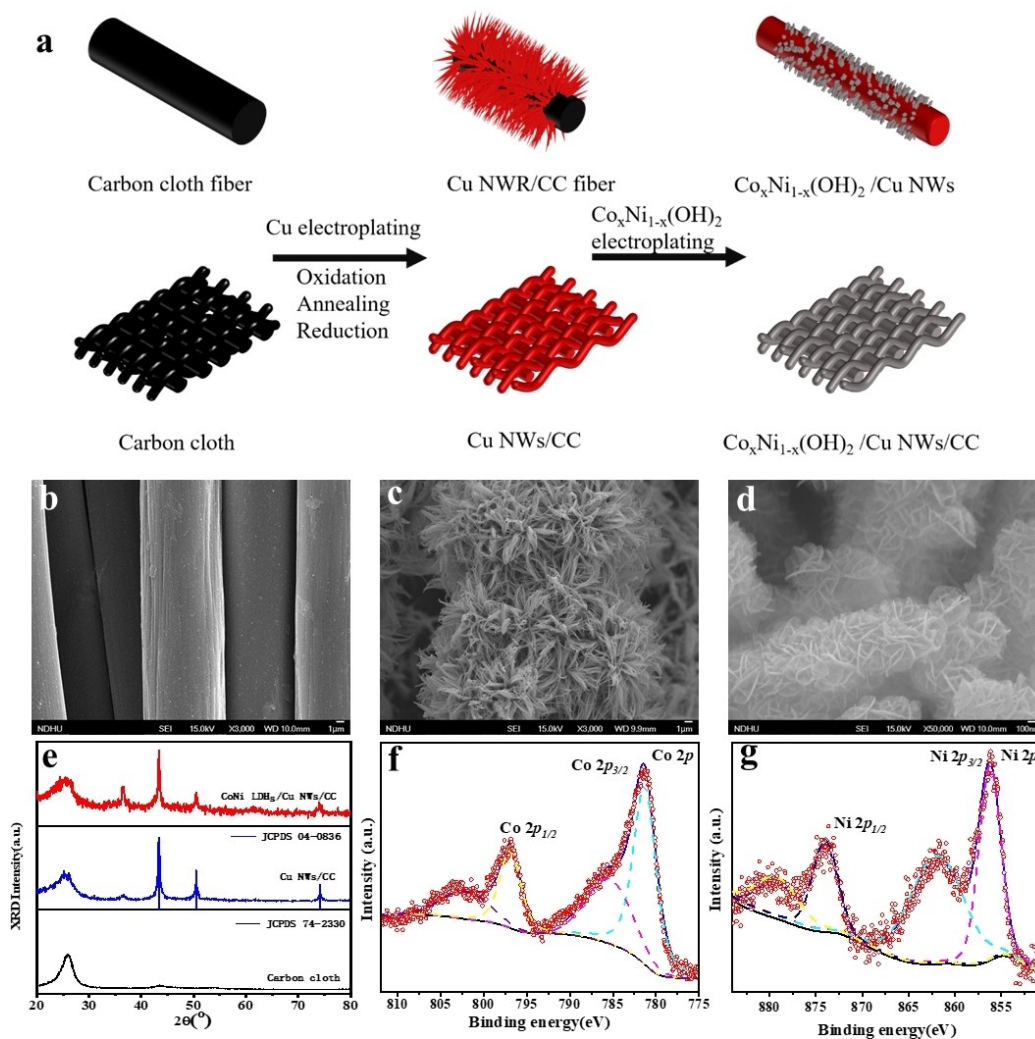

Figure 1. Schematic illustration of the preparation of CoNi-LDHs/Cu NWs/CC. b–d) SEM images of b) CC, c) Cu NWs/CC and d) CoNi-LDHs/Cu NWs/CC. e) XRD patterns of CoNi-LDHs/Cu NWS/CC (red line), Cu NWs/CC (blue line) and CC (black line). f) Co 2p and g) Ni 2p core-level XP spectra of CoNi-LDHs/Cu NWs/CC.

Batteries & Supercaps

Research Article
doi.org/10.1002/batt.202300068

Chemistry
Europe

European Chemical
Societies Publishing

one hand, the surface roughness (Figure 1a). Particularly, at first sight of the carbon fibers in the SEM image of CC, a highly smooth surface is evidently seen and an average diameter $D = {\sim}10\ \mu m$ is further determined. D increases to ${\sim}30\ \mu m$ after the formation of Cu NWs on CC (Figure 1b, c). Such increment unambiguously points to the length of Cu NWs amounting to $L = {\sim}10\ \mu m$ while their diameter $D = {\sim}250\ nm$ is estimated otherwise from another SEM image of Cu NWs in Figure S1(a). Of particular note is the difference between L and D reaching more than one order of magnitude (Figure 1c). Such high aspect ratio of Cu NWs along with the brush-like microstructure of Cu NWs/CC, as a result of Cu NWs standing quasi-vertically on CC, synergistically render the surface roughness of Cu NWs/CC largely enhanced with respect to that of bare CC (Figure 1b, c). As a result, the specific surface area of Cu NWs/CC is markedly increased to facilitate the subsequent precipitation of massive CoNi-LDHs. CoNi-LDHs are characterized by a sheet-like nanostructure with an average thickness $t = {\sim}10\ nm$ and a mean diameter $D = {\sim}150\ nm$ derived from the comparison of the SEM image of CoNi-LDHs/Cu NWs/CC with that of Cu NWs/CC (Figures 1d and S1a). Of particular note are Cu NWs mostly covered conformally with the CoNi-LDHs nanosheets (NSs), leading to the surface roughness of CoNi-LDHs/Cu NWs/CC further augmented with respect to that of Cu NWs/CC (Figures 1d, S1b, S2 and S3). In the meantime, the electrolyte can readily diffuse deeply into Cu NWs/CC, which is benefitted from the numerous mesopores formed between adjacent Cu NWs. Most importantly, those porous channels are substantially preserved after the decoration of Cu NWs/CC with CoNi-LDHs NSs (Figures S1b, S2 and S3). This is in favor of the electrolyte also fluently penetrated throughout the entire CoNi-LDHs/Cu NWs/CC, which is crucial for achieving a good rate capability. In addition to the morphologic transition, a line-shape evolution is further seen via plotting the XRD patterns of CC, Cu NWs/CC and CoNi-LDHs/Cu NWs/CC in parallel for comparison (Figure 1e). Several well-resolved lines at diffraction angle (2θ) of 43.3°, 50.5° and 74.1° emerge after the growth of Cu NWs on CC. Those diffraction lines are indexed to Cu in face-centered cubic (*fcc*) phase (JCPDS card n° 04–0836), of which the relative intensity is evidently higher than that of CC at $2\theta = {\sim}25.6°$. This suggests the good crystallinity of Cu NWs, which is largely preserved after the electrodeposition of CoNi-LDHs on Cu NWs (Figures 1e and S4). Such argumentation is well reinforced in view of those contributions from Cu NWs also clearly manifested in the XRD pattern of CoNi-LDHs/Cu NWs/CC, from which are, however, the characteristic Bragg diffractions of CoNi-LDHs absent. This absence results in the XRD patterns of CoNi-LDHs/Cu NWs/CC and Cu NWs/CC being substantially alike and is attributed presumably to the poor crystallinity of CoNi-LDHs. Their presence is in this regard verified by means of high-resolution transmission electron microscopy (HR-TEM) and XPS (Figures S5 and 1f, g). Figure 1(f) shows the Co 2*p* core-level XP spectrum of CoNi-LDHs/Cu NWs/CC, which is first deconvoluted to give rise to two intense features at binding energy (B.E.) of 781.3 eV and 796.9 eV. That are somewhere between those of the Co $2p_{3/2}$ and Co $2p_{1/2}$ emission lines reported for $Co(OH)_2$ and CoOOH or Co_3O_4 in the literature,

suggesting the co-existence of Co^{2+} and Co^{3+} in CoNi-LDHs.[43] Two extra contributions at B.E. of 785.4 eV and 802.1 eV are further seen, which has been reportedly assigned to the shake-up satellite of the Co $2p_{3/2}$ and Co $2p_{1/2}$ contributions, respectively. More importantly, this implies a majority of cobalt ions in CoNi-LDHs having a divalent state.[44] Alongside is the Ni 2*p* core-level XP spectrum of CoNi-LDHs/Cu NWs/CC, of which the multimodal line-shape is a result of the convolution of four components at B.E. of 856.2, 861.9, 874.0 and 879.2 eV, respectively (Figure 1g). Those characteristics are highly consistent with those of Ni $2p_{3/2}$ and Ni $2p_{1/2}$ emission lines as well as their corresponding shake-up satellites reported for $Ni(OH)_2$ in the literature, passing a clear indication of the divalent state of the nickel ions in CoNi-LDHs.[44,45]

Electrochemical characterization of CoNi-LDHs/Cu NWs/CC

Following the material characterizations are the electrochemical properties of CoNi-LDHs/Cu NWs/CC first examined by means of CV within a potential window of 0 V (vs. Ag/AgCl) to 0.5 V (vs. Ag/AgCl) at various scan rates from $1\ mV\,s^{-1}$ to $5\ mV\,s^{-1}$ (Figure 2a). The measurement was carried out in a three-electrode cell configuration, consisting of CoNi-LDHs/Cu NWs/CC functioned as the working electrode, a Pt sheet as the counter electrode and an Ag/AgCl reference electrode (Figure S6). 1 M NaOH was used as electrolyte. At first sight of the CV curve collected at a scan rate of $1\ mV\,s^{-1}$, a pair of redox peaks is evidently manifested at potentials of ${\sim}0.4$ V (vs. Ag/AgCl) and ${\sim}0.15$ V (vs. Ag/AgCl) (Figure 2a). The charge storage by CoNi-LDHs/Cu NWs/CC is in this regard primarily through the surface or near-surface Faradaic reaction of CoNi-LDHs (Figure S7a).[46] To compensate for the negative charge of stored electrons, positively charged Na^+ has to be intercalated into CoNi-LDHs, leading to the redox reaction kinetics dictated mostly by the solid-state diffusion rate of Na^+ in CoNi-LDHs. Such argumentation is well strengthened in view of the kinetic analysis of the CV curves by the Dunn method,

$$i(V) = k_1\nu + k_2\nu^{0.5} \tag{1}$$

wherein the diffusion-controlled contribution ($k_2\nu^{0.5}$) to the potential-dependent current response ($i(V)$) of CoNi-LDHs/Cu NWs/CC measured at a scan rate (ν) of $1\ mV\,s^{-1}$ amounts to 86.21 % [Figure 2b and Equation (1)]. This by far exceeds that (13.79 %) of the capacitive counterpart ($k_1\nu$) originated otherwise from the non-Faradaic ion adsorption/desorption in the electric double-layer.[47,48] Additional reinforcement to the aforesaid conclusion is given by the EIS Nyquist plots collected at diverse potentials from 0.1 V (vs. Ag/AgCl) to 0.4 V (vs. Ag/AgCl), wherein a Warburg impedance (Z_w) is evidently manifested as a straight line inclined at a constant phase angle in the low-frequency region (Figure 2c). Z_w has been reported associated with the cation diffusion in the electrode.[49] Further analysis of this impedance spike using the complex non-linear least square (CNLS) fitting method based on the equivalent circuit shown in the inset of Figure 2(c) allows the quantifica-
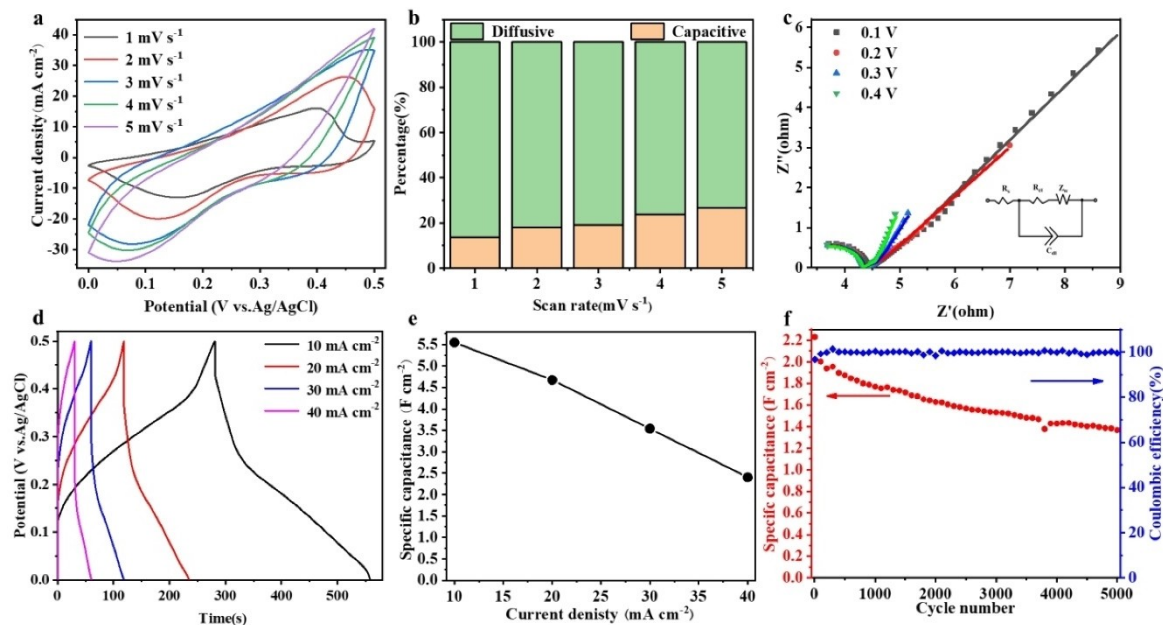
Figure 2. a) CV curves of CoNi-LDHs/Cu NWs/CC. b) Capacitive and diffusion-controlled contributions to charge storage by CoNi-LDHs/Cu NWs/CC. c) EIS Nyquist plots and d) GCD curves of CoNi-LDHs/Cu NWs/CC. e, f) Specific areal capacitance of CoNi-LDHs/Cu NWs/CC as a function of e) current density and f) cycle number at a current density of 40 mA cm^{-2}. The corresponding Coulombic efficiency is also plotted alongside in (f). Inset in (c): Equivalent circuit describing electrochemical behavior of CoNi-LDHs/Cu NWs/CC.

tion of the diffusion resistance (R_w) and the diffusion time constant (τ_d).[50] In addition to R_w and τ_d, the solution resistance (R_s) and the double-layer capacitance (C_{dl}) are also estimated by employing the aforesaid approach to fit the impedance semi-circle in the high-frequency domain, which has been reported in reference to the charge transfer reaction at the electrode/electrolyte interface. Those fitting parameter are summarized in Table 1. Of particular note are R_w and R_{ct} increased when the applied potential on the CoNi-LDHs/Cu NWs/CC electrode gradually decreased from 0.4 V (vs. Ag/AgCl) to 0.1 V (vs. Ag/AgCl). In the meantime, CoNi-LDHs are also progressively reduced to in turn call for the intercalation of Na$^+$ for charge compensation, leading to CoNi-LDHs flooded with numerous Na$^+$. Those inserted Na$^+$ give rise to a strong repulsion to impede the diffusion of additional Na$^+$ into CoNi-LDHs, which thereby hardly further reacts.[51] As a result, R_w and R_{ct} are simultaneously augmented and τ_d is largely shortened from 0.63 s to 0.05 s. Most importantly, no phase transition of CoNi-LDHs is triggered by the aforesaid ion insertion/extraction

process, as unambiguously corroborated by the absence of the voltage plateau from the GCD plots measured for the CoNi-LDHs/Cu NWs/CC electrode at different current densities from 10 mA cm^{-2} to 40 mA cm^{-2} (Figure 2d). In other words, the sluggish rearrangement of the crystal structure of CoNi-LDHs is well circumvented to in turn allow the CoNi-LDHs/Cu NWs/CC electrode under a large charging/discharging current density of 40 mA cm^{-2} yet exhibiting a specific areal capacitance amounting to $C_s = 2.40$ F cm^{-2}. This by far exceeds those reported for additional CoNi-based electroactive materials in the literature [Equation (1) and Figure 2e].[36,52,53] Additional contribution to this good rate performance stems from, on the other hand, the elimination of the insulating binder from the fabrication process of CoNi-LDHs/Cu NWs/CC (Figure 1a). This coupled with the macropores between the carbon fibers and the mesopores between the Cu NWs and the CoNi-LDHs NSs, synergistically ensure facile electron conduction and fluent ion migration throughout the entire electrode (Figures 1b–d, 2e and S7b). Benefitting from such facile charge transport kinetics and the high packing density of CoNi-LDHs in the CoNi-LDHs/Cu NWs/CC electrode, its specific areal capacitance reaches $C_s = 5.55$ F cm^{-2} (corresponding to a gravimetric capacitance of 1209.15 F g^{-1}) at a current density of 10 mA cm^{-2}, again well surpassing those reported in the literature [Equation (1), Figures 1d, S1b, 2e and Table S1].[54–56] The great promise of the CoNi-LDHs/Cu NWs/CC electrode developed in this study is in view of those outperformances and its decent longevity, as reflected in its specific areal capacitance $C_s = 1.40$ F cm^{-2} being still in the order of F cm^{-2} after 5,000 charging/discharging cycles, well attested [Equation (1), Figures 2f and S8].

Table 1. Fitting results of the impedance spectra of the CoNi LDHs/Cu NWs/CC electrode.[a]

Potential [V]	R_s [Ω cm^2]	R_{ct} [Ω cm^2]	R_w [Ω cm^2]	τ_d [σ]	C_{dl} [μF cm^{-2}]
0.1	3.10	1.23	0.91	0.05	1.87
0.2	3.08	1.22	0.79	0.10	1.87
0.3	3.13	1.21	0.70	0.59	1.90
0.4	3.18	1.15	0.65	0.63	1.88

[a] R_s is the solution resistance; R_{ct} is the charge-transfer resistance; R_w is the diffusion resistance; τ_d is the diffusion time coefficient; C_{dl} is the double-layer capacitance.
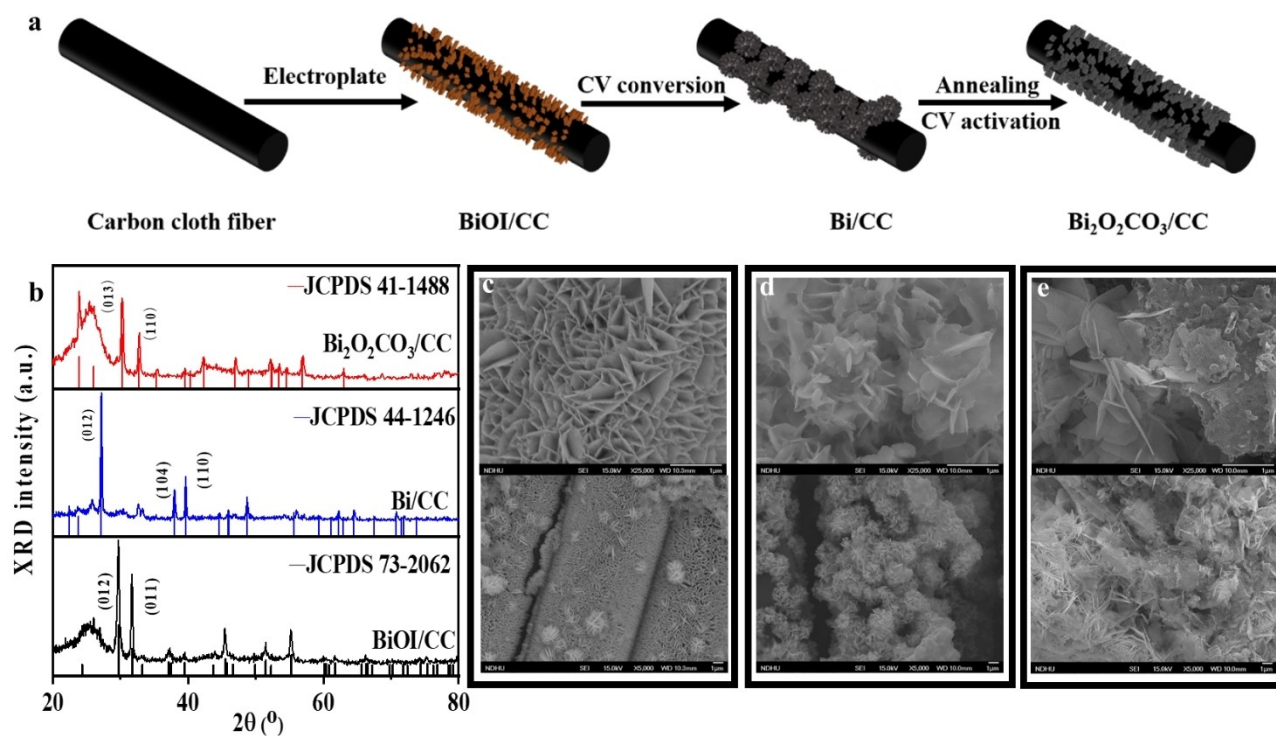
Figure 3. a) Schematic illustration of the preparation of $Bi_2O_2CO_3$/CC. b) XRD patterns of BiOI/CC (black line), Bi/CC (blue line) and $Bi_2O_2CO_3$/CC (red line). c–e) SEM images of c) BiOI/CC, d) Bi/CC and e) $Bi_2O_2CO_3$/CC at high-magnification (top panel) and low-magnification (bottom panel), respectively.

Material and electrochemical characterizations of $Bi_2O_2CO_3$/CC

$Bi_2O_2CO_3$ is preferentially chosen in the present contribution as the negative electrode by taking, on the one hand, its layered crystal structure with large interplanar distance amounting to 0.684 nm into account.[57] This is in favor of the ion intercalation/deintercalation, which is crucial for achieving high C_s. On the other hand, the wide operation potential window (V) of $Bi_2O_2CO_3$ also plays an important role in determining the device performance of a supercapacitor. Herein, the $Bi_2O_2CO_3$ negative electrode is coupled with CoNi-LDHs/Cu NWs/CC functioned as the positive electrode to build a full pseudocapacitor [Equations (2) and (3), and Figure S9]. To this end, $Bi_2O_2CO_3$ is first synthesized by means of electrodeposition of BiOI on CC, which is then transformed into Bi via CV, and eventually giving rise to $Bi_2O_2CO_3$ through post-annealing (Figures 3a and S10). Such argumentation is unambiguously corroborated by their XRD patterns summarized in Figure 3(b). Particularly, the characteristic Bragg diffractions of BiOI in a tetragonal phase (JCPDS card n° 73–2062) are no longer seen after the electrochemical conversion into Bi (Figure 3b). Likewise, the diffraction lines of Bi crystallized into a hexagonal structure (JCPDS card n° 44–1246) are entirely absent from the XRD pattern collected after the post-thermal treatment, wherein all the features are exclusively indexed to tetragonal $Bi_2O_2CO_3$ (JCPDS card n° 41–1488). Despite such a significant change in the crystal structure, as evidently reflected in the line-shape evolution observed from the comparison of the three XRD patterns shown in Figure 3(b), the morphology of BiOI, Bi and $Bi_2O_2CO_3$ are

substantially alike and all characterized by a sheet-like nanostructure (Figure 3c–e). Benefitting from such nanoengineering is the specific surface area of $Bi_2O_2CO_3$ NSs largely increased to allow more Na^+ concurrently intercalated into $Bi_2O_2CO_3$ (Figure S11). Moreover, the diffusion distance is in the meantime markedly shortened. The synergistic effect renders the specific areal capacitance of the $Bi_2O_2CO_3$/CC electrode reaching $C_s = 2.55$ F cm^{-2} (corresponding to a gravimetric capacitance of 404.22 F g^{-1}), which is estimated from the GCD plots shown in Figure 4(a) (Figure 4b). This well outperforms those reported for additional Bi-based electroactive materials in the literature.[58–60] Herein, the measurement was performed likewise in a three-electrode scheme, consisting of $Bi_2O_2CO_3$/CC served as the working electrode, a Pt sheet as the counter electrode, an Ag/AgCl reference electrode and 1 M NaOH used as the electrolyte. More importantly, such outstanding C_s is substantially preserved even if the charging/discharging current density increases from 6 mA cm^{-2} to 10 mA cm^{-2}, which unambiguously highlights the remarkable rate performance of the $Bi_2O_2CO_3$/CC electrode (Figure 4b). Further noteworthy are two voltage plateaus at ~ −0.8 V (vs. Ag/AgCl) and ~ −0.4 V (vs. Ag/AgCl) evidently seen in the GCD plots, suggesting a phase transition of $Bi_2O_2CO_3$ highly likely occurred and most probably induced by the Na^+ insertion into $Bi_2O_2CO_3$ (Supplementary Note 1).[47] Such attribution is well reinforced in view of the kinetic analysis of the CV curves collected within a wide potential window of −1.2 V (vs. Ag/AgCl) to 0 V (vs. Ag/AgCl) at diverse scan rates from 1 mV s^{-1} to 5 mV s^{-1} (Figure 4c, d). Particularly, the diffusion-limited contribution reaches 90.74% to 95.67%, far surpassing that (4.33% to 9.26%) of the capacitive counterpart
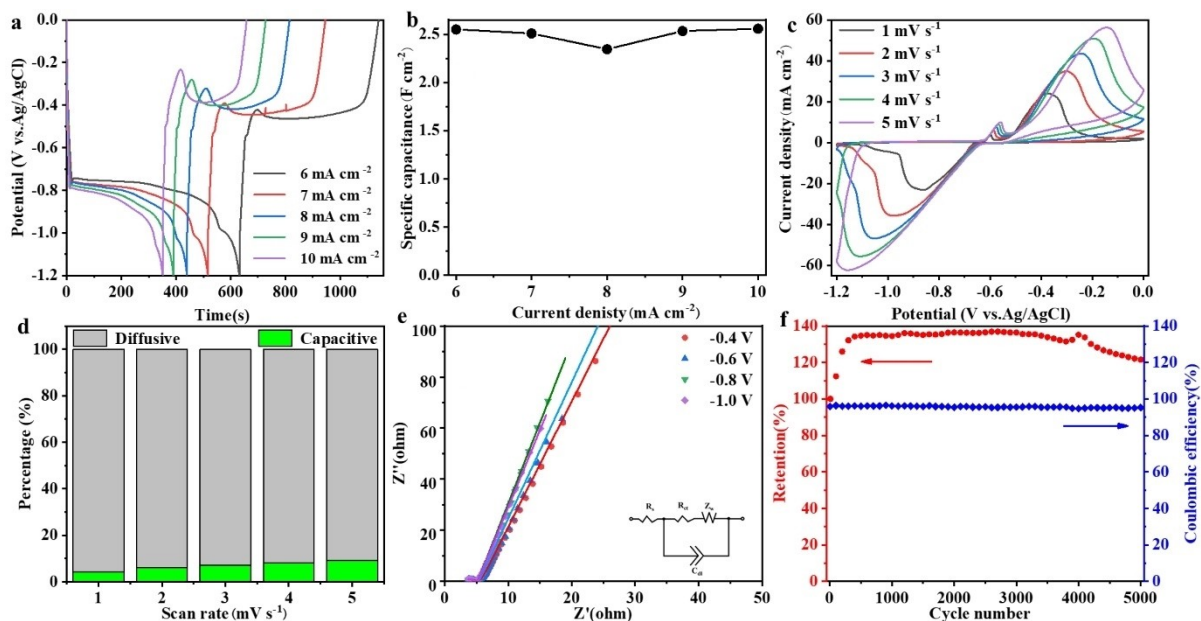
Batteries & Supercaps

Research Article
doi.org/10.1002/batt.202300068

Chemistry Europe
European Chemical
Societies Publishing

Figure 4. a) GCD curves of $Bi_2O_2CO_3$/CC. b) Specific areal capacitance of $Bi_2O_2CO_3$/CC as a function of current density. c) CV curves of $Bi_2O_2CO_3$/CC. d) Capacitive and diffusion-controlled contributions to charge storage by $Bi_2O_2CO_3$/CC. e) EIS Nyquist plots of $Bi_2O_2CO_3$/CC. f) Specific areal capacitance of $Bi_2O_2CO_3$/CC as a function of cycle number at a current density of 20 mA cm^{-2}. The corresponding Coulombic efficiency is also plotted alongside in (f). Inset in (e): Equivalent circuit describing electrochemical behavior of $Bi_2O_2CO_3$/CC.

by nearly one order of magnitude. Such cation intercalation-triggered crystal structure rearrangement is, however, presumably highly kinetically facile in view of, on the one hand, the excellent rate capability of the $Bi_2O_2CO_3$/CC electrode (Figure 4b). On the other hand, the Warburg impedance in the low-frequency region of the EIS Nyquist plots of $Bi_2O_2CO_3$/CC measured at different applied potentials of -1 V (vs. Ag/AgCl) to -0.4 V (vs. Ag/AgCl) is again manifested as a straight line whereas with a phase angle close to 90° (Figure 4e). Recall that this low-frequency impedance branch is related to the cation diffusion in the electrode and its slope has been further reported proportional to the cation diffusion rate.[49] The quasi-vertical impedance spike thus suggests a fast intercalation of Na$^+$ into $Bi_2O_2CO_3$ (Figure 4e). Such argumentation is well reinforced in view of the small diffusion time constant $\tau_d =$ 0.18 s to $\tau_d = 0.24$ s, which is estimated from the EIS Nyquist plots using the CNLS fitting method based on the equivalent circuit shown in the inset of Figure 4(e) (Table 2). This facile ion transport kinetics as presumably a result of the interlayer distance of $Bi_2O_2CO_3$, which amounts to 0.684 nm and more

importantly, by far exceeds the ionic radius of Na$^+$.[61] Its phase transition is in this regard highly reversible, which takes most responsibility for the exceptional stability of the $Bi_2O_2CO_3$/CC electrode, as evidently manifested in the more than 120% retention of its specific areal capacitance after 5,000 charging/discharging cycles (Figures 4f and S12).

Electrochemical characteristics of $Bi_2O_2CO_3$/CC//CoNi-LDHs/Cu NWs/CC pseudocapacitor

Benefitting from the wide potential window $V = 1.2$ V of $Bi_2O_2CO_3$ and that ($V = 0.5$ V) of CoNi-LDHs, the cell voltage of the pseudocapacitor, which builds on $Bi_2O_2CO_3$/CC functioned as the negative electrode and CoNi-LDHs/Cu NWs/CC served as the positive electrode, achieves 1.7 V (Figure 5a, b). This far surpasses the thermodynamic threshold (1.23 V) of water electrolysis by nearly 0.5 V. More importantly, the absence of the current leap at the cut-off voltages from the CV curves of the $Bi_2O_2CO_3$/CC//CoNi-LDHs/Cu NWs/CC pseudocapacitor measured at diverse scan rates from 1 mV s^{-1} to 5 mV s^{-1} unambiguously punctuates the charge leakage from neither $Bi_2O_2CO_3$/CC nor CoNi-LDHs/Cu NWs/CC to the electrolyte (Figure 5b). This leads to its superior coulombic efficiency, as distinctly evidenced by the high symmetry of not only the CV curves but also the GCD plots collected at different current densities from 10 mA cm^{-2} to 30 mA cm^{-2} (Figure 5b, c). From those GCD curves is the specific areal capacitance of the $Bi_2O_2CO_3$/CC//CoNi-LDHs/Cu NWs/CC supercapacitor further determined, which reaches $C_s = 1.08$ F cm^{-2} and slightly decreases to $C_s = 0.92$ F cm^{-2} when the charging/discharging current density is enhanced from 6 mA cm^{-2} to 10 mA cm^{-2}

Table 2. Fitting results of the impedance spectra of the $Bi_2O_2CO_3$/CC electrode.[a]

Potential [V]	R_s [Ω cm^2]	R_{ct} [Ω cm^2]	R_w [Ω cm^2]	τ_δ [σ]	C_{dl} [μF cm^{-2}]
0.1	2.97	1.74	2.82	0.18	1.12
0.2	2.96	1.70	2.16	0.19	1.14
0.3	2.94	1.68	1.63	0.19	1.10
0.4	2.99	1.67	1.54	0.24	1.14

[a] R_s is the solution resistance; R_{ct} is the charge-transfer resistance; R_w is the diffusion resistance; τ_d is the diffusion time coefficient; C_{dl} is the double-layer capacitance.
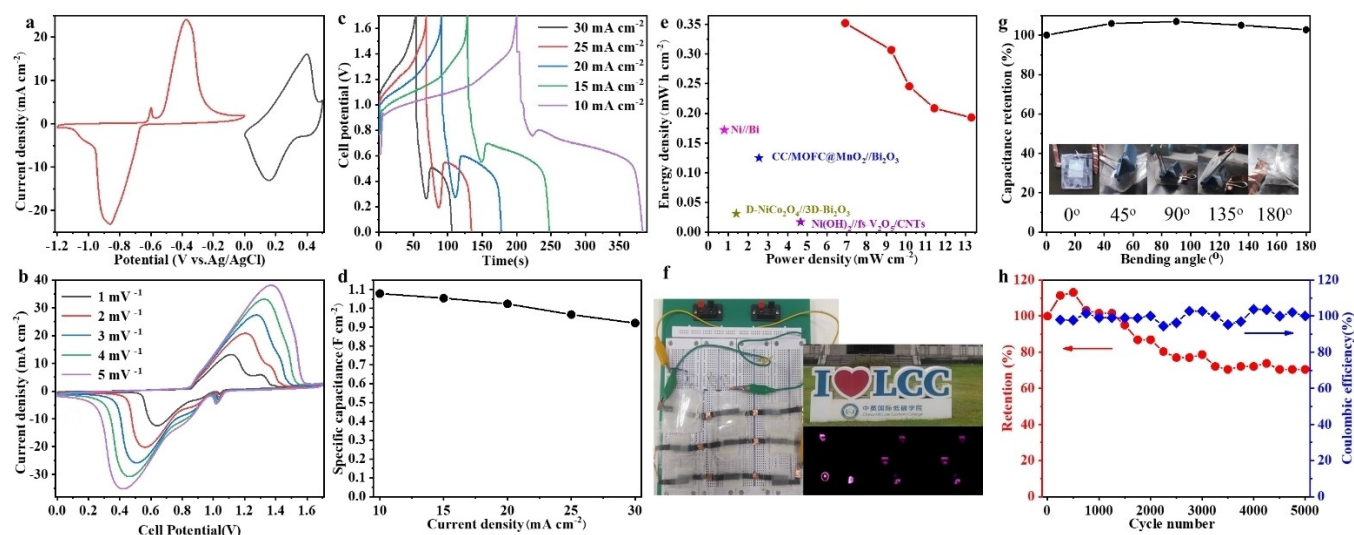
Figure 5. a) CV curves of $Bi_2O_2CO_3$/CC (red line) and CoNi-LDHs/Cu NWs/CC (black line) electrodes measured at a scan rate of 1 mV s^{-1}. b) CV curves and c) GCD plots of $Bi_2O_2CO_3$/CC//CoNi-LDHs/Cu NWs/CC pseudocapacitor. d) Specific areal capacitance of $Bi_2O_2CO_3$/CC//CoNi-LDHs/Cu NWs/CC pseudocapacitor as a function of current density. e) Ragone plot of $Bi_2O_2CO_3$/CC//CoNi-LDHs/Cu NWs/CC pseudocapacitor. The value reported for additional energy storage devices are added for comparison.[62–65] f) Photo of quasi-solid-state $Bi_2O_2CO_3$/CC//CoNi-LDHs/Cu NWs/CC pseudocapacitors connected in series to power an array of LED lamps arranged in a "LCC" pattern. g, h) Specific areal capacitance of $Bi_2O_2CO_3$/CC//CoNi-LDHs/Cu NWs/CC pseudocapacitor as a function of g) bending angle and h) cycle number at a current density of 80 mA cm^{-2}. The corresponding Coulombic efficiency is also plotted alongside in (h).

(Figure 5c, d). This good rate performance is benefitted to a large extent from the synergistic effect of the facile ion and electron transport throughout the $Bi_2O_2CO_3$/CC and CoNi-LDHs/Cu NWs/CC electrodes. This has already been discussed in great detail in the previous paragraphs and more importantly, further renders the power and energy densities of the $Bi_2O_2CO_3$/CC//CoNi-LDHs/Cu NWs/CC pseudocapacitor amounting to $P = 13.31$ mW cm^{-2} and $E = 0.35$ mWh cm^{-2}, respectively (Figure 5e). Such superior E and P, as clearly highlighted by the comparison with those reported for additional pseudo- and hybrid-capacitors in the literature using the Ragone plot, are substantially preserved even if the $Bi_2O_2CO_3$/CC//CoNi-LDHs/Cu NWs/CC supercapacitor is fabricated in a quasi-solid-state device using a NaOH/PVA gel as the electrolyte. Such argumentation is well attested by its capability of simultaneously lighting up an array of indicators containing 9 LED lamps arranged in a "LCC" pattern via series connection with eight additional entities (Figure 5f).[62–65] Those outstanding device performances unambiguously punctuate its great promise as an energy-rich and highly stable power source (Figure 5e, f). Such argumentation is further reinforced in view of, on the one hand, its good flexibility, as evidently reflected in the absence of the capacitance loss even if the $Bi_2O_2CO_3$/CC//CoNi-LDHs/Cu NWs/CC pseudocapacitor is strongly distorted (Figure 5g). On the other hand, its decent durability, as explicitly corroborated by more than 70 % capacitance retention after 5,000 charging/discharging cycles, further strengthens its good prospect for practical application in portable and wearable electronics (Figure 5h).

Conclusions

The use of Cu NWs/CC as an alternative current collector to the conventional metal foil shows exceptional potential for the fabrication of supercapacitor electrode with electroactive material at high mass loading. This is ascribed to its large specific surface area resulted from the Cu NWs standing quasi-vertically on CC, which in favor of the massive deposition of electrode material. This is exemplified in the present contribution using CoNi-LDHs in view of its ultrahigh theoretical capacitance. As an additional consequence of the Cu NWs directly grown on CC is the formation of three-dimensional (3D) conductive percolation network to facilitate the electron readily transferred from Cu NWs/CC to the CoNi-LDHs. Moreover, CoNi-LDHs are particularly engineered into a sheet-like nanostructure. Numerous mesopores are formed between those CoNi-LDHs NSs, which along with those between the Cu NWs and the macropores between the carbon fibers of CC collectively give rise to a hierarchical porous structure to promote the ions fluently penetrated throughout the entire CoNi-LDHs/Cu NWs/CC electrode. The synergistic effect of such facile charge transport kinetics renders the CoNi-LDHs/Cu NWs/CC electrode exhibiting outstanding rate capability, as evidently manifested in its specific areal capacitance amounting to $C_s = 5.55$ F cm^{-2} (corresponding to a gravimetric capacitance of 1209.15 F g^{-1}) even at a high charging/discharging current density of 10 mA cm^{-2}. Such outstanding C_s well outperforms those reported for additional CoNi-based electroactive materials. More importantly, benefitting from such outstanding rate performance, the asymmetric supercapacitor built on CoNi-LDHs/Cu NWs/CC as the positive electrode coupled with $Bi_2O_2CO_3$/CC as the negative electrode also demonstrate remarkable power density $P = 13.31$ mW cm^{-2} while its energy

Batteries & Supercaps

Research Article
doi.org/10.1002/batt.202300068

Chemistry Europe
European Chemical
Societies Publishing

density reaches $E = 0.35$ mWh cm^{-2}. The great promise of the $Bi_2O_2CO_3$/CC//CoNi-LDHs/Cu NWs/CC supercapacitor developed in this study is in view of such superior performance well attested and further reinforced by its potential application as an energy-dense power source for portable and wearable electronics. This is exemplified herein first using a NaOH/PVA gel electrolyte to fabricate the quasi-solid-state device to power the LED lamp. The discussions insofar unambiguously punctuate the electrode design put forward in the present contribution well addressing the conflict between the high mass loading and efficient utilization of the electroactive materials in the electrode. Such blueprints can be readily generalized to energy storage devices for enhancing their energy and power densities simultaneously.

Experimental

Materials

Copper acetate ($Cu(CH_3COO)_2$), sulfuric acid (H_2SO_4), acetic acid (CH_3COOH), sodium hydroxide (NaOH), potassium bicarbonate ($KHCO_3$), cobalt nitrate ($Co(NO_3)_2$), nickel nitrate ($Ni(NO_3)_2$), bismuth nitrate pentahydrate ($Bi(NO_3)_3 \cdot 5H_2O$), p-benzoquinone ($C_6H_4O_2$), ethanol (C_2H_5OH), potassium iodide (KI), nitric acid (HNO_3), glucose ($C_6H_{12}O_6$), polyvinyl alcohol (PVA, $M_W = 84000–89000$), and lactic acid ($CH_3CH(OH)COOH$) were purchased from Shanghai Titan Scientific Co., Ltd., China. Carbon cloth (designation W0S1002, basic weight 120 g m^{-2}, thickness 0.33 mm, no wet-proofing) was purchased from CeTech Co., Ltd., Taiwan. All reagents were of analytical grade and used as received without any further purification.

Fabrication of CoNi-LDHs/Cu NWs/CC electrode

Prior to the synthesis, CC was cut into a small piece with a geometric area of 0.5 cm × 2 cm and used as the working electrode. CC is further coupled with a platinum (Pt) foil (1.5 cm × 1.5 cm) as the counter electrode and an Ag/AgCl reference electrode in 3 M KCl (0.207 V vs. the standard hydrogen electrode, SHE) to build a three-electrode cell. An aqueous solution containing 0.02 M Cu-($CH_3COO)_2$ was utilized as the electrolyte for the direct growth of Cu on CC (Cu/CC) by means of electroplating at a constant bias of -2 V (vs. Ag/AgCl) for 20 min. As-obtained Cu/CC was next converted into $Cu(OH)_2$ NWs/CC by means of electrochemical oxidation in 1 M NaOH at 4 °C in a two-electrode configuration, consisting of Cu/CC as the working electrode and a Pt sheet as the counter electrode. A constant current of 4.5 mA was then applied to Cu/CC for 20 min. As-prepared $Cu(OH)_2$ NWs/CC was then subject to post-annealing in air at 180 °C for 60 min for dehydration, giving rise to CuO NWs/CC. CuO NWs/CC further experienced electroreduction in 1 M $KHCO_3$ at a constant applied potential of -1 V (vs. Ag/AgCl) for 5 min to transform into Cu NWs/CC. The conversion was carried out in a three-electrode scheme, comprising CuO NWs/CC as the working electrode, a Pt foil as the counter electrode and an Ag/AgCl reference electrode in 3 M KCl. The subsequent electrodeposition of CoNi LDHs on Cu NWs/CC was also carried out in a highly analogous three-electrode setup except for employing an aqueous solution containing 0.1 M $Co(NO_3)_2$ and 0.1 M $Ni(NO_3)_2$ as the electrolyte and Cu NWs/CC as the working electrode. An external bias of -1 V (vs. Ag/AgCl) was then applied to Cu NWs/CC for 2 min. As-synthesized CoNi LDHs/Cu NWs/CC was eventually rinsed several times with distilled water

to remove residual precursors and naturally dried under ambient condition. The mass loading of CoNi LDHs is determined by means of inductively coupled plasma mass spectrometry (ICP-MS) to be ~4.59 mg cm^{-2}.

Fabrication of $Bi_2O_2CO_3$/CC electrode

In the present study, $Bi_2O_2CO_3$ was derived from the bismuth oxyiodide (BiOI), which was first electrodeposited on CC (0.5 cm × 2 cm).[66] A reaction reservoir, which comprised 0.23 M p-benzoquinone dissolved in 20 mL ethanol as well as 0.04 M $Bi(NO_3)_3 \cdot 5H_2O$, 0.4 M KI and 0.03 M lactic acid dissolved in distilled water with pH adjusted to 1.7 by HNO_3, was employed. The electrodeposition was initiated by applying a strong bias of -0.35 V (vs. Ag/AgCl) to CC as the working electrode for 15 s, which was coupled with a Pt sheet as the counter electrode and an Ag/AgCl reference electrode in a three-electrode configuration. Afterwards, the applied potential on CC was reduced to -0.1 V (vs. Ag/AgCl) to support the growth of BiOI for 2 h. As-obtained BiOI/CC was next converted into Bi/CC by means of cyclic voltammetry (CV) in a potential window of -1.2 to -0.2 V (vs. Ag/AgCl) at a scan rate of 10 mV s^{-1} for 20 cycles. Bi/CC was then immersed in an aqueous solution containing 1 M glucose for 5 min. The glucose-coated Bi/CC electrode was subsequently subject to post-thermal treatment in nitrogen (N_2) atmosphere at 650 °C for 120 min to eventually give rise to $Bi_2O_2CO_3$/CC, which was further rinsed several times with distilled water and naturally dried under ambient condition. The mass loading of $Bi_2O_2CO_3$ is determined by means of ICP-MS to be ~6.31 mg cm^{-2}.

Assembly of asymmetric $Bi_2O_2CO_3$/CC//CoNi-LDHs/Cu NWs/CC pseudocapacitor with gel electrolyte

A piece of filter paper along with as-prepared $Bi_2O_2CO_3$/CC and as-synthesized CoNi LDHs/Cu NWs/CC were altogether immersed into 1 M NaOH gel electrolyte for 5 min. This gel electrolyte was prepared following the recipe reported in the literature and described here in brief.[67] 4 g PVA was first added to 40 mL deionized water and stirred at 85 °C for 4 h to allow PVA fully dissolved in water, to which was then 1.65 g NaOH added and stirred to form a jelly-like solution. The filter paper then served as the separator and was sandwiched between $Bi_2O_2CO_3$/CC functioned as the negative electrode and CoNi LDHs/Cu NWs/CC worked as the positive electrode, which altogether are naturally dried under ambient condition and eventually sealed in parafilm foil to give rise to the $Bi_2O_2CO_3$/CC//CoNi LDHs/Cu NWs/CC supercapacitor.

Material and electrochemical characterizations

X-ray diffraction (XRD) was performed on a Bruker D8 advanced diffractometer using Ge-monochromated Cu $K_{\alpha1}$ radiation with a wavelength of 0.1540598 nm. Scanning electron microscopy (SEM) was carried out on a Jeol JEM-4000EX electron microscope operated at an accelerating voltage of 15 kV. X-ray photoelectron spectroscopy (XPS) was conducted on a Perkin Elmer PHI 1600 ECSA system with the binding energy (B.E.) calibrated using the C 1s photoelectron peak at 284.6 eV as reference. All the electrochemical measurements including CV, galvanostatic charge/discharge (GCD) and electrochemical impedance spectroscopy (EIS) were implemented on a CHI 6273D potentiostat/galvanostat. EIS was performed over a frequency range of 10 mHz to 10 kHz at an amplitude of 10 mV.

Batteries & Supercaps

Research Article
doi.org/10.1002/batt.202300068

Chemistry Europe
European Chemical
Societies Publishing

Calculations

Specific areal capacitance (C_s/F cm^{-2}) of $Bi_2O_2CO_3$/CC and CoNi LDHs/Cu NWs/CC was estimated from their corresponding GCD curves using the equation shown below [Equation (2)].[68]

$$C_s = \frac{I \times \Delta t}{\Delta V \times A} \qquad (2)$$

In this expression, I/A is the applied current, Δt/s refers to the discharging time, ΔV/V corresponds to the potential window for the scan, and A/cm^2 denotes the working area of the electrode, respectively. Specific areal energy (E_s/mWh cm^{-2}) and power densities (P_s/mW cm^{-2}) of the $Bi_2O_2CO_3$/CC//CoNi LDHs/Cu NWs/CC supercapacitor was likewise calculated from the collected GCD curve via the following formulae,

$$E_s = \frac{I \int V \mathrm{d}t}{3.6 \times A} \qquad (3)$$

$$P_s = \frac{3600 \times E_s}{\Delta t} \qquad (4)$$

wherein V/V stands for the potential of the discharge curve integrated with respect to time t/s [Equations (3) and (4)].[69]

Supporting Information

The authors have cited additional references within the Supporting Information.[70–81]

Acknowledgements

Conflict of Interests

The authors declare no conflict of interest.

Data Availability Statement

The data that support the findings of this study are available from the corresponding author upon reasonable request.

[1] D. P. Dubal, N. R. Chodankar, D. H. Kim, P. Gomez-Romero, *Chem. Soc. Rev.* **2018**, *47*, 2065–2129.
[2] Q. M. Jiang, M. R. Zhang, L. Q. Luo, G. B. Pan, *Talanta* **2017**, 250–254.
[3] S. Wa Ng, W. Li, H. Song, C. Mao, Z. Zhang, H. Peng, G. Li, *Inorg. Chem. Front.* **2019**, *6*, 1275–1281.
[4] W. Zhang, Y. Wang, X. Guo, Y. Liu, Y. Zheng, M. Zhang, R. Li, Z. Peng, Z. Wang, T. Zhang, *J. Alloys Compd.* **2021**, *855*, 157394.
[5] S. Jiang, M. Pang, R. Liu, J. Song, R. Wang, N. Li, Q. Pan, H. Yang, W. He, J. Zhao, *J. Alloys Compd.* **2022**, *895*, 162451.
[6] L. Zhu, J. Dong, H. Zhang, C. Xu, X. Zhao, Y. Yao, Q. Zeng, *J. Alloys Compd.* **2021**, *856*, 158204.
[7] L. Demarconnay, E. Raymundo-Piñero, F. Béguin, *J. Power Sources* **2011**, *196*, 580–586.
[8] Y. Huang, L. Quan, T. Liu, Q. Chen, D. Cai, H. Zhan, *Nanoscale* **2018**, *10*, 14171–14181.
[9] G. A. Snook, P. Kao, A. S. Best, *J. Power Sources* **2011**, *196*, 1–12.
[10] W. Hong, L. Wang, K. Liu, X. Han, Y. Zhou, P. Gao, R. Ding, E. Liu, *J. Alloys Compd.* **2018**, *746*, 292–300.
[11] N. S. Shaikh, S. B. Ubale, V. J. Mane, J. S. Shaikh, V. C. Lokhande, S. Praserthdam, C. D. Lokhande, P. Kanjanaboos, *J. Alloys Compd.* **2022**, *893*, 161998.
[12] G. Zan, T. Wu, P. Hu, Y. Zhou, S. Zhao, S. Xu, J. Chen, Y. Cui, Q. Wu, *Energy Storage Mater.* **2020**, *28*, 82–90.
[13] J. Xu, Z. Meng, Z. Hao, X. Sun, H. Nan, H. Liu, Y. Wang, W. Shi, H. Tian, X. Hu, *J. Colloid Interface Sci.* **2022**, *609*, 878–889.
[14] L. Xie, S. Chen, Y. Hu, Y. Lan, X. Li, Q. Deng, J. Wang, Z. Zeng, S. Deng, *J. Alloys Compd.* **2021**, *858*, 157652.
[15] J. Wang, S. Sarwar, J. Song, L. Du, T. Li, Y. Zhang, B. Li, Q. Guo, J. Luo, X. Zhang, *J. Alloys Compd.* **2022**, *892*.
[16] Y. Gogotsi, P. Simon, *Science* **2011**, *334*, 917–918.
[17] Y. Zhang, X. Liu, G. Wang, Y. Li, S. Zhang, D. Wang, H. Sun, *J. Alloys Compd.* **2020**, *825*, 154020.
[18] J. Sun, Z. Li, J. Wang, W. Hong, P. Gong, P. Wen, Z. Wang, S. Yang, *J. Alloys Compd.* **2015**, *642*, 231–238.
[19] L. Hu, W. Chen, X. Xie, N. Liu, Y. Yang, H. Wu, Y. Yao, M. Pasta, H. N. Alshareef, Y. Cui, *ACS Nano* **2011**, *5*, 8904–8913.
[20] N. Wang, X. Zhang, Z. Ju, X. Yu, Y. Wang, Y. Du, Z. Bai, S. Dou, G. Yu, *Nat. Commun.* **2021**, *12*, 4519.
[21] Z. Zhao, M. Sun, W. Chen, Y. Liu, L. Zhang, N. Dongfang, Y. Ruan, J. Zhang, P. Wang, L. Dong, Y. Xia, H. Lu, *Adv. Funct. Mater.* **2019**, *29*, 1809196.
[22] M. Li, K. Y. Ma, J. P. Cheng, D. Lv, X. B. Zhang, *J. Power Sources* **2015**, *286*, 438–444.
[23] P. Sun, Z. Li, L. Zhang, C. Dong, Z. Li, H. Yao, J. Wang, G. Li, *J. Alloys Compd.* **2018**, *750*, 607–616.
[24] Ragupathi, M. Ulaganathan, *J. Alloys Compd.* **2021**, *888*, 161453.
[25] Y. Kuang, C. Chen, D. Kirsch, L. Hu, *Adv. Energy Mater.* **2019**, *9*, 1901457.
[26] J. Xu, J. Lei, N. Ming, C. Zhang, K. Huo, *Adv. Funct. Mater.* **2022**, *32*, 2204426.
[27] X. Zhang, Z. Ju, Y. Zhu, K. J. Takeuchi, E. S. Takeuchi, A. C. Marschilok, G. Yu, *Adv. Energy Mater.* **2020**, *2000808*.
[28] J. Ma, J. Li, R. Guo, H. Xu, F. Shi, L. Dang, Z. Liu, J. Sun, Z. Lei, *J. Power Sources* **2019**, *428*, 124–130.
[29] D. Guo, Y. Luo, X. Yu, Q. Li, T. Wang, *Nano Energy* **2014**, *8*, 174–182.
[30] X. Liu, W. Xu, D. Zheng, Z. Li, Y. Zeng, X. Lu, *J. Mater. Chem. A* **2020**, *8*, 17938–17950.
[31] S. Raj, S. K. Srivastava, P. Kar, P. Roy, *Electrochim. Acta* **2019**, *302*, 327–337.
[32] H.-H. Joo, C. V. V. M. Gopi, R. Vinodh, H.-J. Kim, S. Sambasivam, I. M. Obaidat, *J. Energy Storage* **2019**, *26*, 100914.
[33] X. Pu, X. Ren, H. Yin, Y. Tang, H. Yuan, *J. Alloys Compd.* **2021**, *865*, 158736.
[34] M. Jing, H. Hou, C. Banks, Y Yang, Y Zhang, X Ji, *ACS Appl. Mater. Interfaces* **2015**, *7*, 22741–22744.
[35] M. Jing, C. Wang, H. Hou, Z. Wu, Y. Zhu, Y. Yang, X. Jia, Y. Zhang, X. Ji, *J. Power Sources* **2015**, *298*, 241–248.
[36] Q. Chen, J. Jin, Z. Kou, Z. Jiang, Y. Fu, Z. Liu, L. Zhou, L. Mai, *J. Mater. Chem. A* **2020**, *8*, 13114–13120.
[37] H.-Y. Sun, L.-Y. Lin, Y.-Y. Huang, W.-L. Hong, *Electrochim. Acta* **2018**, *281*, 692–699.
[38] Z.-H. Huang, F.-F. Sun, M. Batmunkh, W.-H. Li, H. Li, Y. Sun, Q. Zhao, X. Liu, T.-Y. Ma, *J. Mater. Chem. A* **2019**, *7*, 11826–11835.
[39] J. Wang, J. Gong, H. Zhang, L. Lv, Y. Liu, Y. Dai, *J. Alloys Compd.* **2021**, *870*, 159466.

[40] G. Maheshwaran, P. Pandi, S. Suganya, B. A. Kumar, G. Ramalingam, M. R. Prabhu, S. Sudhahar, *J. Energy Storage* **2022**, *56*, 105900.

[41] R. Liu, L. Ma, G. Niu, X. Li, E. Li, Y. Bai, G. Yuan, *Adv. Funct. Mater.* **2017**, *27*, 1701635.

[42] L. Ma, T. Zhao, F. Xu, T. You, X. Zhang, *Chem. Eng. J.* **2021**, *405*, 126694.

[43] Y. Zhang, L. Xue, C. Liang, Y. Chen, J. Liu, C. Shen, Q. Li, Y. Duan, L. Yao, H. Zhang, Y. Cai, C. Tan, Z. Luo, *Appl. Surf. Sci.* **2021**, *561*, 150079.

[44] J. Liang, R. Ma, N. Iyi, Y. Ebina, K. Takada, T. Sasaki, *Chem. Mater.* **2009**, *22*, 371–378.

[45] Y. Fu, J. Song, Y. Zhu, C. Cao, *J. Power Sources* **2014**, *262*, 344–348.

[46] H. Gholipour-Ranjbar, M. Soleimani, H. R. Naderi, *New J. Chem.* **2016**, *40*, 9187–9193.

[47] V. Augustyn, P. Simon, B. Dunn, *Energy Environ. Sci.* **2014**, *7*, 1597–1614.

[48] H. S. Kim, J. B. Cook, H. Lin, J. S. Ko, S. H. Tolbert, V. Ozolins, B. Dunn, *Nat. Mater.* **2017**, *16*, 454–460.

[49] J. Ye, Z. Li, Z. Dai, Z. Zhang, M. Guo, X. Wang, *J. Electron. Mater.* **2016**, *45*, 4237–4245.

[50] X. F. Sánchez-Romate, A. D. Bosque, J. Artigas-Arnaudas, B. K. Muñoz, M. Sánchez, A. Ureña, *Electrochim. Acta* **2021**, *370*, 137746.

[51] T. Zhai, X. Lu, Y. Ling, M. Yu, G. Wang, T. Liu, C. Liang, Y. Tong, Y. Li, *Adv. Mater.* **2014**, *26*, 5869–5875.

[52] X. F. Gong, J. P. Cheng, K. Y. Ma, F. Liu, L. Zhang, X. Zhang, *Mater. Chem. Phys.* **2016**, *173*, 317–324.

[53] C. Shi, H. Cao, S. Li, L. Guo, Y. Wang, J. Yang, *J. Energy Storage* **2022**, *54*, 105270.

[54] Y. Chen, B. Xu, J. Wen, J. Gong, T. Hua, C. W. Kan, J. Deng, *Small* **2018**, *14*, 1704373.

[55] Y. Liu, S. Guo, W. Zhang, W. Kong, Z. Wang, W. Yan, H. Fan, X. Hao, G. Guan, *Electrochim. Acta* **2019**, *317*, 551–561.

[56] D. Zhao, X. Wu, C. Guo, *Inorg. Chem. Front.* **2018**, *5*, 1378–1385.

[57] B. Wang, J. Wang, Y. Zhang, Y. Mei, P. Lian, *Ceram. Int.* **2017**, *43*, 9310–9316.

[58] H. Sun, G. Yang, J. Chen, C. Kirk, N. Robertson, *J. Mater. Chem. C* **2020**, *8*, 13253–13262.

[59] J. Wen, S. Sun, B. Zhang, N. Shi, X. Liao, G. Yin, Z. Huang, X. Chen, X. Pu, *RSC Adv.* **2019**, *9*, 4693–4699.

[60] J. Chen, U. T. Nakate, Q. T. Nguyen, S. Park, *Ceram. Int.* **2022**, *48*, 22417–22425.

[61] P. Zhang, Y. Rao, Y. Huang, M. Chen, T. Huang, W. Ho, S. Lee, J. Zhong, J. Cao, *J. Chem. Eng.* **2021**, *420*, 129814.

[62] A. Xl, A. Bx, B. Xz, C. A. Feng, A. Jh, H. A. Qin, A. Wl, *Appl. Surf. Sci.* **2020**, *515*, 145977.

[63] X. Liu, C. Guan, Y. Hu, L. Zhang, A. M. Elshahawy, J. Wang, *Small* **2017**, *1702641*.

[64] S. A. Kumar, A. Mohanty, B. Saravanakumar, S. Mohanty, S. K. Nayak, A. Ramadoss, *ChemComm* **2020**, 12973–12976.

[65] C. Shi, J. Sun, Y. Pang, Y. Liu, B. Huang, B. T. Liu, *J. Colloid Interface Sci.* **2022**, *607*, 462–469.

[66] Y. Ma, X. Jiang, R. Sun, J. Yang, X. Jiang, Z. Liu, M. Xie, E. Xie, W. Han, *Chem. Eng. J.* **2020**, *382*, 123020.

[67] H. Zhang, H. Su, L. Zhang, B. Zhang, F. Chun, X. Chu, W. He, W. Yang, *J. Power Sources* **2016**, *331*, 332–339.

[68] G. Zhu, H. Wen, M. Ma, W. Wang, L. Yang, L. Wang, X. Shi, X. Cheng, X. Sun, Y. Yao, *Chem. Commun. (Camb.)* **2018**, *54*, 10499–10502.

[69] S. Zhang, N. Pan, *Adv. Energy Mater.* **2015**, *5*, 1401401.

[70] W. Ye, P. Ye, H. Wang, F. Chen, Y. Zhong, Y. Hu, *J. Colloid Interface Sci.* **2022**, *612*, 298–307.

[71] C. M. McShane, K.-S. Choi, *Phys. Chem. Chem. Phys.* **2012**, *14*, 6112–6118.

[72] I. Platzman, R. Brener, H. Haick, R. Tannenbaum, *J. Phys. Chem. C* **2008**, *14*, 1101–1108.

[73] Z. Yuan, H. Wang, J. Shen, P. Ye, J. Ning, Y. Zhong, Y. Hu, *J. Mater. Chem. A* **2020**, *8*, 22163–22174.

[74] Y.-L. Liu, Y. Cheng, G.-G. Wang, H.-Y. Zhang, L.-Y. Dang, B.-W. Wu, Z.-Q. Lin, X.-S. An, J.-C. Han, *ACS Appl. Mater. Interfaces* **2019**, *11*, 9984–9993.

[75] J.-X. Feng, L.-X. Ding, S.-H. Ye, X.-J. He, H. Xu, Y.-X. Tong, G-R. Li, *Adv. Mater.* **2015**, *27*, 7051–7057.

[76] X. Tong, D. Wu, C. Zhang, K. Lian, D. Xiong, S. Xu, Y. Zhu, R. Qi, R. Huang, L. Wang, P. K. Chu, *J. Mater. Chem. A* **2017**, *5*, 2629–2639.

[77] H. Wang, Y. Yang, Q. Li, W. Lu, J. Ning, Y. Zhong, Z. Zhang, Y. Hu, *Sci. China Mater.* **2021**, *64*, 840–851.

[78] M. Jing, H. Hou, C. Banks, Y Yang, Y Zhang, X Ji, *ACS Appl. Mater. Interfaces* **2015**, *7*, 22741–22744.

[79] M. Wei, Q. Huang, Y. Zhou, Z. Peng, W. Chu, *J. Energy Chem.* **2018**, *27*, 591–599.

[80] L. Jiang, Y. Sui, J. Qi, Y. Chang, Y. He, Q. Meng, F. Wei, Z. Sun, Y. Jin, *Appl. Surf. Sci.* **2017**, 148–159.

[81] Y. Li, L. Shan, Y Sui, J. Qi, F. Wei, Y. He, Q. Meng, Y. Ren, J Liu, *J. Mater. Sci. Mater. Electron.* **2019**, *30*, 13360–13371.